remote sensing

MDPI

Article

A High-Precision Monitoring Method for Surface Subsidence in Western Chinese Mining Areas by Fusing InSAR and LiDAR

Dayong Xu [1,2,†], Tao Wei [1,3,†], Lei Wang [1,3,*], Jingyu Li [4], Shenshen Chi [1,3] and Xiaohan Liu [1]

[1] School of Geomatics, Anhui University of Science and Technology, Huainan 232001, China; xdy9958@163.com (D.X.)
[2] Cathay Safety Technology Co., Ltd., Beijing 102299, China
[3] State Key Laboratory for Safe Mining of Deep Coal Resources and Environment Protection, Anhui University of Science and Technology, Huainan 232001, China
[4] School of Geoscience and Surveying and Mapping Engineering, China University of Mining and Technology-Beijing, Beijing 100083, China
* Correspondence: austwlei@163.com
† These authors contributed equally to this work.

Highlights

What are the main findings?

- A LiDAR echo-based non-growing surface feature extraction method is proposed to suppress vegetation interference, providing stable and consistent monitoring targets for subsidence retrieval in vegetated mining areas.
- A fusion boundary partitioning strategy is constructed using InSAR deformation gradient and image coherence, combined with inverse mean squared error weighted fusion; the proposed method achieves centimeter-level accuracy across the entire subsidence basin, retaining high precision in both large-gradient centers and small-gradient edges, reducing the full-gradient RMSE to 39 mm—91% lower than InSAR and 30% lower than LiDAR.

What are the implications of the main findings?

- The non-growing surface feature extraction scheme effectively improves monitoring stability for western Chinese mining areas with complex terrain and dense vegetation, ensuring reliable deformation observation under strong vegetation interference.
- The proposed InSAR and LiDAR fusion method overcomes the inherent limitations of single remote sensing techniques, establishing a scalable technical framework for full-gradient subsidence monitoring and supporting ecological security and safe mining in ecologically fragile coal-producing regions.

Abstract

Surface subsidence monitoring in western Chinese mining areas is challenged by complex topography, dense vegetation, and large deformation gradients. Traditional single remote sensing methods suffer from inherent drawbacks: InSAR performs well in small-gradient areas but is prone to incoherence in large-gradient zones, whereas LiDAR achieves high accuracy in large-gradient monitoring but lacks precision for small-gradient deformations. This study proposes a high-precision monitoring method by fusing InSAR and LiDAR data. First, a non-growing surface feature extraction approach using LiDAR echo characteristics is adopted to reduce vegetation noise and improve monitoring stability. Second, fusion boundaries are determined using InSAR corrected deformation gradient and image coherence, dividing the subsidence basin into small-, medium-, and large-gradient zones. Third, an inverse mean squared error weighted fusion strategy is applied in the medium-gradient

Check for updates

Academic Editor: Michele Saroli

Received: 25 March 2026
Revised: 30 April 2026
Accepted: 5 May 2026
Published: 12 May 2026

Copyright: © 2026 by the authors. Licensee MDPI, Basel, Switzerland. This article is an open access article distributed under the terms and conditions of the Creative Commons Attribution (CC BY) license.

zone to realize reliable data integration. Experiments conducted at the Sihe Coal Mine show that the full-gradient RMSE of InSAR is 415 mm, and that of LiDAR is 56 mm. The proposed fusion method reduces the full-gradient RMSE to 39 mm, which is 91% lower than that of InSAR and 30% lower than that of LiDAR. The method achieves centimeter-level accuracy across the entire subsidence basin while maintaining high precision in both large-gradient centers and small-gradient edges. It provides a stable and practical technical solution for full-gradient subsidence monitoring in western Chinese mining areas with complex terrain and dense vegetation.

Keywords: surface subsidence; InSAR; LiDAR; weighted fusion; high-precision monitoring

1. Introduction

As the world's largest developing country, China has long maintained an energy consumption structure dominated by coal [1–3]. With the gradual depletion of coal resources in the eastern plains, the western region, rich in coal reserves, is becoming the core of China's coal mining [4–6]. Statistics show that over one-third of China's coal mines are distributed in western mountainous areas [7]. Coal mining inevitably damages underground rock structures. In western mountainous areas, the complex topography and fragile geology mean that rock structure damage not only triggers ecological issues like soil erosion and vegetation degradation but also threatens local lives and properties [8–10]. Against this backdrop, achieving high-precision real-time monitoring and scientific prediction of surface deformation during mountain coal mining has become an urgent technical challenge, crucial for ensuring regional ecological security and sustainable development.

As an important spaceborne earth observation technology, InSAR (Interferometric Synthetic Aperture Radar) has demonstrated significant advantages and application potential in mine subsidence monitoring, owing to its all-day, all-weather operation and wide-area coverage [11–13]. Unlike traditional monitoring methods, InSAR inverts surface deformation from radar image phase information, enabling continuous dynamic monitoring of large areas regardless of time and space constraints. This non-contact approach enhances monitoring efficiency and cost-effectiveness, reducing manpower and material investment, thus becoming a research hotspot in mine monitoring. Scholars have made progress in InSAR applications: Benedetta A et al. [14] applied conventional and advanced DInSAR to monitor mining subsidence in Poland, identifying 30 subsidence troughs and measuring cumulative subsidence over 70 cm with velocities up to 50 mm/year. Wang et al. [15] further optimized mine InSAR monitoring using a PUNet (Phase Unwrapping Network) and M-estimation-based robust sequential adjustment, boosting calculation efficiency and reducing anomaly errors. Quan et al. [16] combined InSAR with dual-channel and single-view methods to monitor 3D surface deformation in Huainan's Guqiao Mine, verifying InSAR's applicability for mining subsidence inversion. Long et al. [17] addressed numerical model limitations and insufficient InSAR data mining by fusing deep learning, improving the prediction accuracy of surface deformation. Zhang et al. [18] applied InSAR to Hunan coalfield subsidence monitoring, reconstructing typical mine subsidence processes and identifying hazard locations to support geological disaster prevention. However, mine-induced ground subsidence typically features high subsidence rates, large deformations, and discontinuous spatial distributions [19], posing challenges to InSAR monitoring.

As an advanced remote sensing technology, LiDAR (Light Detection and Ranging), with its high precision, efficiency, and unique 3D spatial information acquisition capability, has demonstrated significant advantages in topographic mapping and engineering

surveying [20–22]. Compared with traditional methods, it rapidly acquires 3D ground point cloud data via laser pulse scanning, not only penetrating vegetation to obtain high-precision topography for fine complex terrain modeling but also enabling efficient data collection to shorten the acquisition cycle, thus making it widely applied in engineering. In coal mine subsidence monitoring, scholars have made progress using airborne LiDAR: Ordóñez et al. [23] verified that iPad Pro 11 LiDAR achieves higher accuracy than traditional surveying in Ecuadorian underground mines, providing a low-cost tool for artisanal and small-scale mining. Yang et al. [24] identified limitations of conventional techniques and noise issues in traditional LiDAR point cloud processing, proposing a local flat point extraction (LFPE) algorithm based on topographic features to achieve high-precision subsidence modeling and horizontal displacement extraction, improving accuracy by over 50%. Zheng et al. [25] constructed a DSuM (digital subsidence model) using LiDAR to solve shallow coal seam deformation detection accuracy challenges in mountainous areas, obtaining high-precision subsidence parameters via point cloud registration, filtering, DEM (Digital Elevation Model) generation, and differencing for mine safety assessment. Despite these achievements, airborne LiDAR faces challenges in mine subsidence monitoring.

In recent years, due to the inherent limitations of single remote sensing techniques, multi-source data fusion has become an important approach to improve the reliability of mining subsidence monitoring. Various integrated methods have been developed. Pawluszek-Filipiak K et al. [26] fused DInSAR and SBAS based on Kriging to monitor mining subsidence in flat plain areas dominated by urban and agricultural land, achieving centimeter-level accuracy. Zhu et al. [27] proposed a fusion method combining D-InSAR, SBAS, and UAV tilt photogrammetry for plain mining areas covered by farmland and villages, realizing zoned collaborative monitoring with reliable precision. Although these methods have improved monitoring performance to varying degrees, most fusion strategies are developed for relatively flat terrain and moderate vegetation conditions. They show insufficient adaptability in the complex environment of western Chinese mining areas, where large deformation gradients, rugged topography, and dense vegetation commonly coexist. Traditional fusion strategies rarely consider the spatial variation of deformation gradients and coherence attenuation, resulting in limited stability and accuracy over the full subsidence basin.

In this context, the study selects two-phase airborne LiDAR data and 12 scenes of InSAR data from typical western Chinese mining areas, utilizes airborne LiDAR echo characteristics and InSAR maximum deformation gradient, integrates the data using the grid method and C2C algorithm, and proposes a high-precision monitoring method for western Chinese mining area subsidence integrating InSAR and LiDAR, aiming to achieve high-precision, full-area dynamic monitoring of surface subsidence in western Chinese mining areas.

2. Basic Principle

2.1. LiDAR Subsidence Extraction Basic Principle

Under complex terrain, ground points obtained by traditional filtering barely support direct deformation monitoring, thus requiring accurate screening of effective point clouds suitable for monitoring or delineation of stable monitoring areas prior to extraction [28,29]. For this reason, surface features in mining areas are classified into two categories: non-growing surface features and growing surface features. Non-growing surface features refer to features unaffected by seasonal growth, mainly manifested as roads, buildings, and bare ground in mines. Growing surface features are those affected by seasonal growth, such as crops and forests in mining areas. In western Chinese mining areas, the terrain is complex, and growing surface features exhibit

higher coverage. Due to seasonal growth effects, LiDAR data for growing surface features have poor temporal stability, making direct deformation monitoring difficult. In contrast, non-growing surface features are unaffected by seasonal growth, with deformation primarily driven by underground mining, and their LiDAR data shows high temporal stability, making them suitable for deformation monitoring in mining areas. As shown in Figure 1, LiDAR sensors contacting non-growing surface features yield single echoes, while penetrating growing surface features produce multiple echoes [30]. Therefore, non-growing surface features can be extracted by leveraging the multiple echo characteristics of growing surface features.

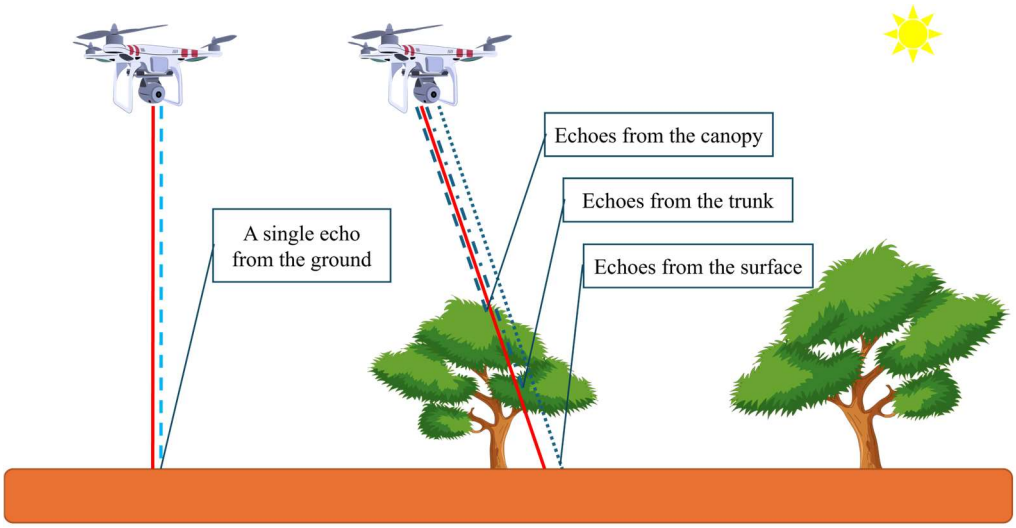


Figure 1. Schematic of multiple echoes in the airborne LiDAR system.

For the multiple echoes of growing surface features, the grid method [31] is applied to partition the LiDAR point cloud (Figure 2). First, denoising preprocessing is performed on the two-phase LiDAR point cloud data; the denoised point cloud is then divided into regular grid cells, and the total point count M and multiple echo count N are statistically analyzed for each grid. By calculating the ratio N/M and comparing it with a preset threshold, grids with N/M exceeding the threshold are excluded. Finally, the C2C algorithm [32] is used to process the two-phase point clouds of non-growing surface features, enabling the extraction of surface subsidence information from non-growing surface features. The specific method flow is shown in Figure 3.

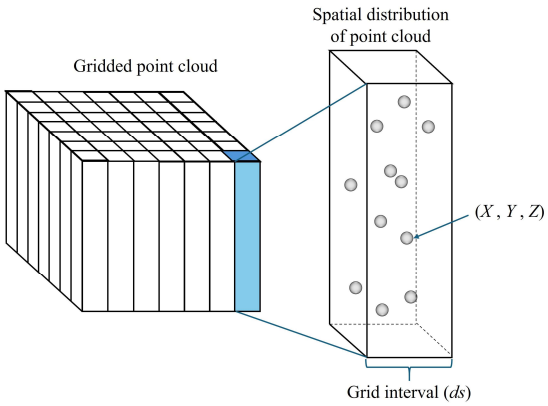


Figure 2. Schematic of virtual grid.

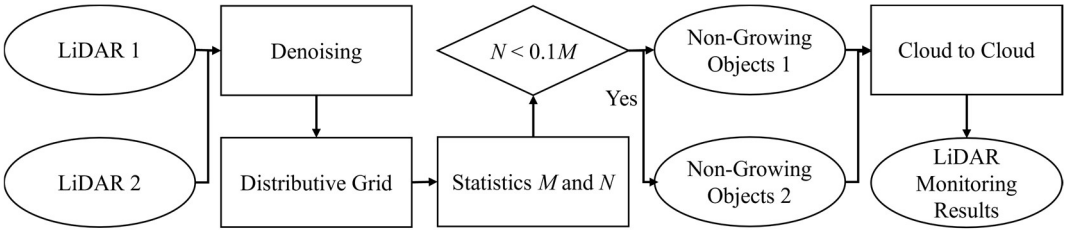


Figure 3. Flowchart for extracting non-growing surface features.

Meanwhile, according to the third law of geography and the spatial continuity characteristics of surface subsidence [33], it can be assumed that the amount of subsidence within the grid is homogeneous under the fine grid scale. The screened non-growing surface feature grids were homogenized to construct the subsidence basin model.

$$H = \sum_{i=1}^{M-N} Z_i / M, \tag{1}$$

where H is the average elevation value of the grid; Z_i is the elevation value of each point in the grid.

2.2. DInSAR Subsidence Extraction Basic Principle

InSAR uses SAR phase information to achieve high-precision three-dimensional imaging of the ground, which can obtain high-precision terrain data and realize large-scale and long-term surface micro-deformation monitoring. It is a key technology for surface change monitoring. On the basis of InSAR, DInSAR extracts deformation information through image interference and difference. It combines external DEM to separate terrain phase, and finally solves the surface deformation [34,35].

The phase obtained by InSAR is related to radar parameters, antenna position, antenna incident angle and ground target elevation. The interference process is affected by a variety of error factors, resulting in the interference phase information not only contains elevation and deformation information, but also other interference terms.

$$\varphi = \varphi_d + \varphi_f + \varphi_t + \varphi_a + \varphi_n, \tag{2}$$

in the formula, φ_d is the deformation phase, φ_f is the flat phase, φ_t is the terrain phase, φ_a is the atmospheric delay phase, and φ_n is the noise phase.

After removing all kinds of interference to obtain the deformation phase φ_d, the surface deformation along the radar line of sight can be quantified by the following formula:

$$d_{los} = \frac{\lambda}{4\pi} \times \varphi_d, \tag{3}$$

in the formula, d_{los} is the surface deformation along the radar line of sight, and λ is the radar wavelength.

After obtaining the deformation d_{los} along the radar line of sight using InSAR, the following formula can be used to convert it into vertical deformation:

$$d_v = \frac{d_{los}}{\cos\theta}, \tag{4}$$

in the formula, d_v is the deformation in the vertical direction; θ is the incidence angle of radar.

2.3. Fusion of InSAR and LiDAR for Subsidence Monitoring

InSAR can monitor small-gradient deformations at the edge of mine subsidence, but has monitoring blind zones in large-gradient deformation areas at the subsidence center. LiDAR, conversely, excels in monitoring large-gradient deformations at the subsidence center but lacks accuracy in small-gradient deformations at the edge. Thus, fusing InSAR and LiDAR enables complementary deformation monitoring, facilitating the construction of a complete and accurate subsidence basin. The key challenge in this fusion is defining the upper and lower fusion boundaries to divide the subsidence area into large-, medium-, and small-gradient deformation zones. Precise boundary definition is the core premise for seamless data integration and synergistic interpretation of the two technologies.

Given that InSAR inverses surface displacement from phase differences between pixels, its monitoring capability has a theoretical upper limit. Massonnet et al. [36] first proposed the concept of deformation gradient, deriving the theoretical formula for InSAR's maximum detectable deformation gradient based on interferometric phase principles.

$$d = \frac{\lambda}{2\mu}, \tag{5}$$

where d is the maximum deformation gradient, μ is the pixel resolution, and λ is the radar wavelength.

Equation (5) indicates that the maximum deformation gradient is positively correlated with the radar wavelength and negatively correlated with the pixel resolution. There are significant differences in the maximum deformation gradient monitorable by different sensors. Take the Sentinel-1 (effective pixel spacing μ = 20 m after multilook processing) and ALOS (effective pixel spacing μ = 10 m after multilook processing) sensors as examples: the theoretical maximum deformation gradient of Sentinel data after 1:4 multiview processing is 1.4×10^{-3}, while that of ALOS data after 1:3 multiview processing reaches 11.5×10^{-3}. The deformation gradient model in Equation (5) is proposed without considering external error sources, assuming no noise in radar images. In practice, however, interferograms are often contaminated by noise from orbital errors, spatiotemporal decorrelation, and atmospheric delays, leading to InSAR's measurable deformation gradient being significantly lower than the theoretical value. For this reason, Baran et al. [37] established a correction model with coherence as the independent variable by correlating the deformation gradient and coherence.

$$D_{\max} = d + 0.002(\gamma - 1), \tag{6}$$

where $D_{\max}$ is the corrected maximum deformation gradient monitorable by InSAR, and γ is the image coherence.

Equation (6) indicates that InSAR's maximum monitorable deformation gradient is linearly and positively correlated with image coherence. Take the Sentinel sensor as an example: when image coherence is below 0.3, Sentinel fails to monitor surface deformation; when coherence equals 1, the model reduces to Massonnet's theoretical maximum deformation gradient formulation. Thus, Baran's function model not only inherits the original definition in form but also extends deformation gradient theory to practical applications. The formula is simple and highly practical.

InSAR data processing involves multiple interferometric pairs, inverting InSAR's maximum measurable deformation gradient $D_{\max}$ from Equation (6), and calculating

the maximum deformation $d_{\max|\mathrm{InSAR}}$ monitorable by multiple interferometric pairs using Equation (7).

$$d_{\max|\mathrm{InSAR}} = \mu \times D_{\max} \times N = \mu \times \left(d + 0.002\left(\gamma_{avg} - 1\right)\right) \times N, \tag{7}$$

where N is the number of interferometric pairs and γ_{avg} is the average coherence coefficient of N interferometric pairs.

The $d_{\min|\mathrm{LiDAR}}$ is a key parameter derived from LiDAR deformation monitoring. It is defined as the average subsidence value along the mining area boundary, extracted from non-growing surface features. Two-phase point clouds of non-growing surface features, identified by LiDAR echo characteristics, are processed using the C2C algorithm. The subsidence values at the mining boundary are then averaged to obtain $d_{\min|\mathrm{LiDAR}}$. Unlike $d_{\max|\mathrm{InSAR}}$, which represents the maximum deformation gradient detected by InSAR, $d_{\min|\mathrm{LiDAR}}$ characterizes the average subsidence at the mining boundary. This boundary corresponds to areas with relatively small deformation gradients and minimal subsidence within the mining subsidence basin. Because it is derived from non-growing surface features with high temporal stability and low sensitivity to seasonal vegetation changes, $d_{\min|\mathrm{LiDAR}}$ ensures reliable estimation of boundary subsidence.

In this study, considering the dual characteristics of high vegetation coverage and rapid, large-magnitude deformation in mining areas, stricter coherence requirements are necessary for effective deformation information extraction. Therefore, $d_{\max|\mathrm{InSAR}}$ is defined as the lower fusion boundary, while $d_{\min|\mathrm{LiDAR}}$ is used as the upper fusion boundary. Based on these two parameters, the subsidence basin is divided into three zones: a small-gradient zone monitored by InSAR, a large-gradient zone monitored by LiDAR, and a medium-gradient zone processed through weighted fusion. This zoning strategy enables effective integration of InSAR and LiDAR deformation data, thereby improving the accuracy of comprehensive deformation analysis in high-vegetation-coverage mining areas.

To ensure the effectiveness of the weighted fusion method, leveling points with subsidence within the interval from $d_{\max|\mathrm{InSAR}}$ to $d_{\min|\mathrm{LiDAR}}$ are selected. The absolute errors between InSAR/LiDAR monitoring values and leveling data are calculated respectively; the cumulative mean square deviation is then calculated, and corresponding weights are calculated using Equations (8) and (9). These fusion thresholds are empirically derived from the study area dataset and are site-specific, not universally transferable constants. The implementation of InSAR and LiDAR weighted fusion monitoring is shown in Figure 4.

$$\begin{array}{l} \frac{P_{\mathrm{InSAR}}}{P_{\mathrm{LiDAR}}} = \frac{\sigma^2_{\mathrm{LiDAR}}}{\sigma^2_{\mathrm{InSAR}}} \\ P_{\mathrm{InSAR}} + P_{\mathrm{LiDAR},} = 1 \end{array}, \tag{8}$$

$$d = \begin{cases} d_{\mathrm{InSAR}} & d < d_{\max|\mathrm{InSAR}} \\ P_{\mathrm{InSAR}} \times d_{\mathrm{InSAR}} + P_{\mathrm{LiDAR}} \times d_{\mathrm{LiDAR}} & d_{\max|\mathrm{InSAR}} \le d \le d_{\min|\mathrm{LiDAR}} \\ d_{\mathrm{LiDAR}} & d > d_{\min|\mathrm{LiDAR}} \end{cases}, \tag{9}$$

where P_{InSAR} and P_{LiDAR} are the corresponding weights, $\sigma^2{}_{\mathrm{InSAR}}$ and $\sigma^2{}_{\mathrm{LiDAR}}$ are the corresponding cumulative root mean square, d_{InSAR} and d_{LiDAR} are the corresponding subsidence values.

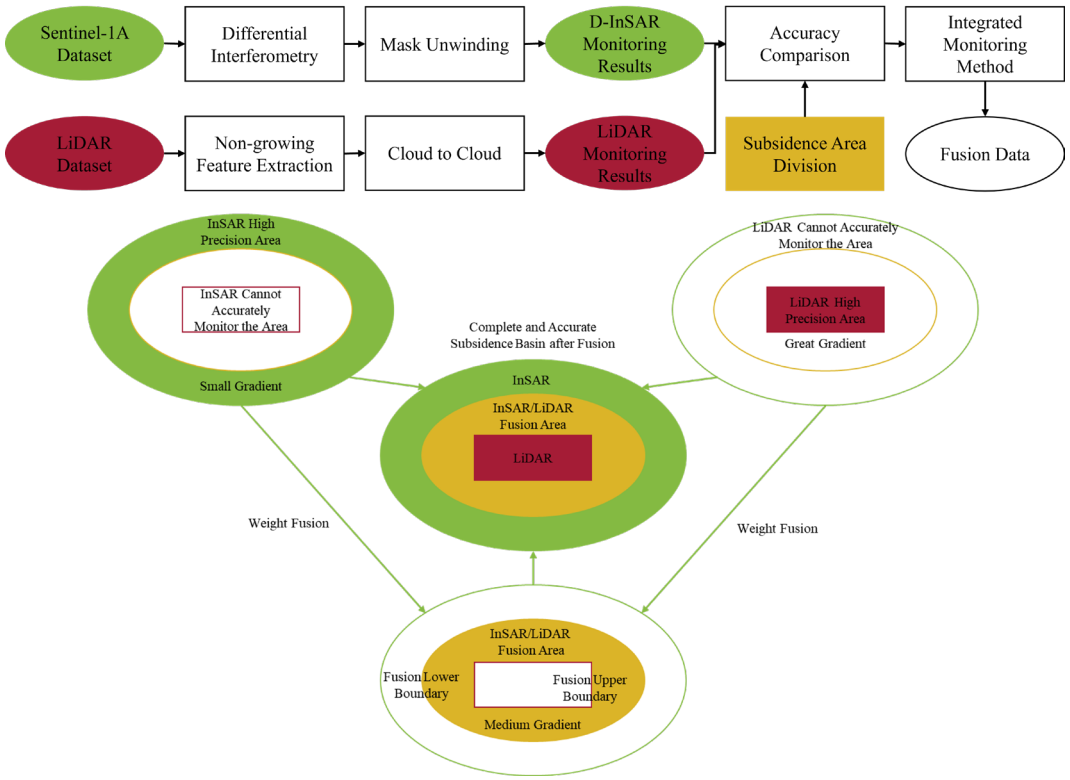


Figure 4. Scheme of InSAR and LiDAR weighted fusion method for subsidence basin monitoring.

3. Engineering Experiment

3.1. Overview of the Study Area and Data

The study selected the Sihe Coal Mine in Jincheng City, Shanxi Province, China. The coal mine is owned by Jinneng Holding Equipment Manufacturing Group and is administratively located in Chuandi Town, Qinshui County. The working face has a strike length of 1145 m, an inclined width of 220 m, an average surface elevation of 985 m, and an average coal seam depth of 514 m. The study area is characterized by complex topography, large elevation differences, abundant vegetation, and terraced fields. Meanwhile, a mountain highway runs through the area, and 123 monitoring points (96 points along the strike and 27 points along the inclination) were set up along its extension for convenient monitoring. Since the end of January 2024, the working face has been retreating at an average rate of 4.9 m per day, advancing a total of 740 m by 22 June 2024. Figure 5 shows the geographic overview of the study area.

The radar data for InSAR analysis are Sentinel-1A ascending-orbit SLC (Single Look Complex) data from the ESA (European Space Agency, Paris, France), with imaging mode IW, polarization VV (Vertical–Vertical Polarization), and imaging time spanning 18 January to 22 June 2024. Relevant parameters are listed in Table 1. POD (Precision Orbit) files were used to attenuate orbital phase errors, 30 m resolution DEM data from NASA (National Aeronautics and Space Administration, Washington, DC, USA) for reference terrain phase removal, and GACOS (Generic Atmospheric Correction Online Service) files from Newcastle University for generalized atmospheric corrections. LiDAR data were acquired using a DJI MATRICE 350 RTK (Real-Time Kinematic) UAV (Unmanned Aerial Vehicle) (DJI, Shenzhen, China) equipped with an EasyScan X10 LiDAR system. Two-phase point cloud acquisitions were conducted on 23 January and 22 June 2024, using fixed route spacing, scanning angle, and pulse frequency parameters to ensure time-series data comparability. Image control point coordinates were obtained via high-precision static measurements, based on which the LiDAR point cloud was

geometrically corrected. LiDAR acquisition details are listed in Table 2, and the UAV platform and survey area topography are shown in Figure 6. Based on the acquisition times of LiDAR campaigns and InSAR images, surface movement data along the strike and dip lines were selected for the period from 20 January to 22 June 2024. The data were obtained from five campaigns of third-order leveling, with an average interval of 30 days. These data provide a reliable foundation for InSAR–LiDAR data fusion.

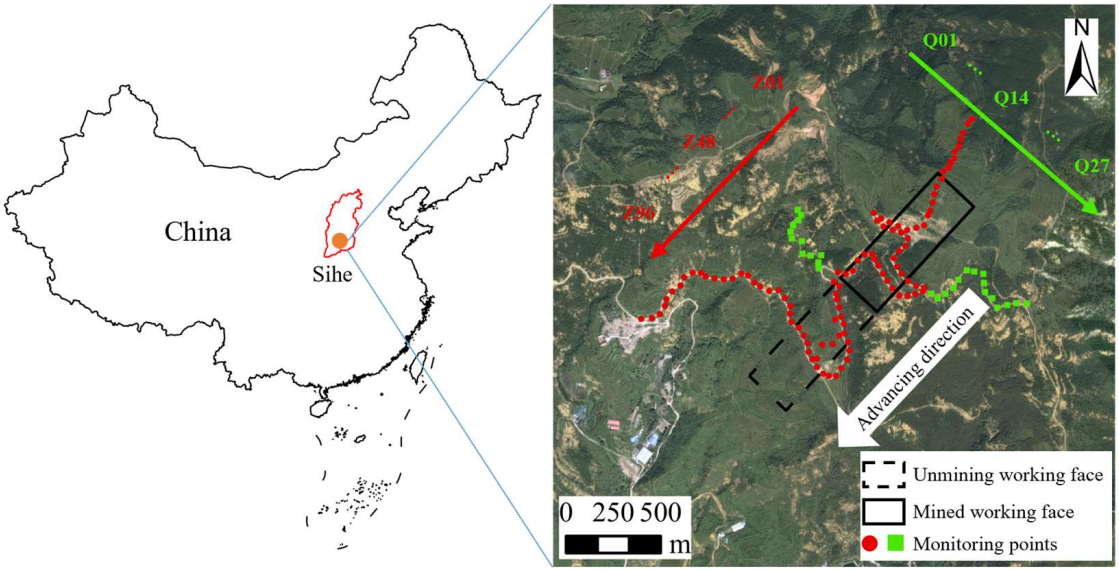


Figure 5. Schematic of working face position and observation line layout.

Table 1. Sentinel-1A SAR interferometric pairs.

No.	Primary Image	Auxiliary Image	Temporal Baseline/d	Spatial Baseline/m
1	18 January 2024	30 January 2024	12	−101.3
2	30 January 2024	11 February 2024	12	79.5
3	11 February 2024	23 February 2024	12	−31.7
4	23 February 2024	6 March 2024	12	−21.9
5	6 March 2024	18 March 2024	12	−30.2
6	18 March 2024	30 March 2024	12	−27.5
7	30 March 2024	11 April 2024	12	129.4
8	11 April 2024	23 April 2024	12	−171.4
9	23 April 2024	5 May 2024	12	−142
10	5 May 2024	17 May 2024	12	15.9
11	17 May 2024	10 June 2024	24	196.6
12	10 June 2024	22 June 2024	12	−9.8

Table 2. LiDAR data acquisition parameters for working faces.

Collection Time	Total Points	Point Cloud Density (Points/m^2)	Percentage of First Echo/%
23 January 2024	400,089,407	60	95.92
22 June 2024	700,012,932	100	95.98



Figure 6. DJI MATRICE 350 RTK UAV and flight area topography.

3.2. Mine Subsidence Monitoring Results and Analysis

3.2.1. InSAR Monitoring Results and Analysis

As shown in Table 1, 12 interferometric pairs were constructed using the DInSAR technique based on Sentinel-1A data to extract surface deformation. To minimize the influence of atmospheric disturbances, the majority of the selected pairs had a temporal baseline of 12 days, and an enhanced Goldstein filter (window size 128, maximum alpha = 3) was applied to the differential interferograms to suppress phase noise caused by mountainous terrain, vegetation cover, and environmental noise, thus yielding the filtered differential interferometric phase map and coherence coefficient map (Figures 7 and 8). With regard to orbital errors, precise orbit data were imported during processing, and more than 10 ground control points located in areas far from the deformation zone with high coherence and smooth unwrapping were manually selected. Residual orbital ramps were effectively removed using a third-order polynomial refinement method. The core processing parameters were set as follows: for interferogram generation, range and azimuth looks were 7 and 2; the Goldstein method was used for interferogram filtering; the Minimum Cost Flow algorithm was adopted for phase unwrapping with an unwrapping coherence threshold of 0.3; the Polynomial Refinement method with a polynomial degree of 3 was employed for orbital refinement; and the product coherence threshold for phase-to-displacement conversion was set to 0.3. All parameters were configured in accordance with the standard SARscape workflow, ensuring the reproducibility of the experiment.

As can be seen from Figure 7, during the early mining stage (January to March), the interference fringes are relatively distinct. With the gradual advancement of the working face, the interference fringes show a shifting trend. Based on this phenomenon, it can be preliminarily determined that surface subsidence occurred in the study area during the research period, which is most likely induced by underground mining activities. Combined with Figure 8, it can be observed that the 2nd, 5th, and 6th interferometric pairs exhibit high coherence, with clear and continuous interference fringe structures in the differential interferograms, which can accurately reflect the spatial characteristics of surface deformation. However, the 7th and 8th interferograms are contaminated by considerable noise accompanied by severe decorrelation.

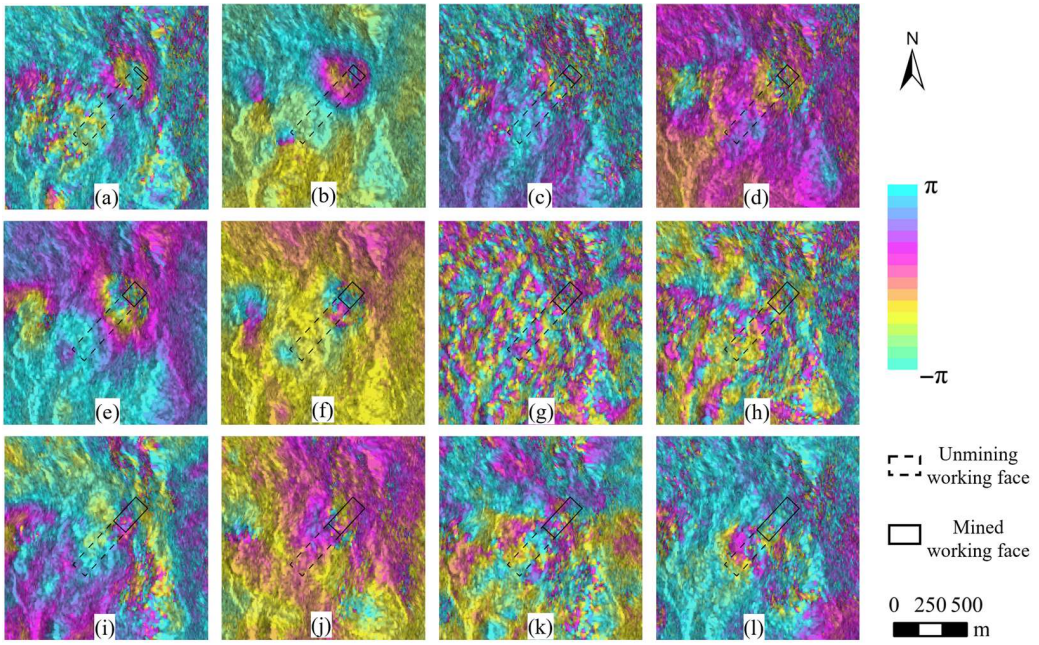


Figure 7. Differential interferogram after filtering: (**a**) Differential interferogram of Pair No. 1; (**b**) Differential interferogram of Pair No. 2; (**c**) Differential interferogram of Pair No. 3; (**d**) Differential interferogram of Pair No. 4; (**e**) Differential interferogram of Pair No. 5; (**f**) Differential interferogram of Pair No. 6; (**g**) Differential interferogram of Pair No. 7; (**h**) Differential interferogram of Pair No. 8; (**i**) Differential interferogram of Pair No. 9; (**j**) Differential interferogram of Pair No. 10; (**k**) Differential interferogram of Pair No. 11; (**l**) Differential interferogram of Pair No. 12.

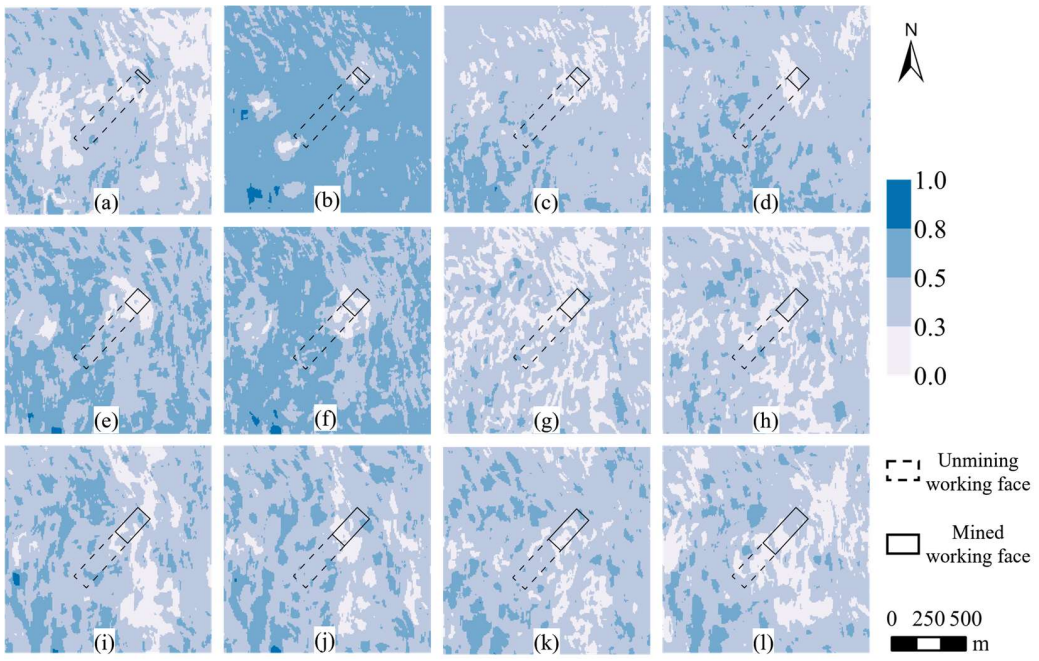


Figure 8. Coherence coefficient diagram: (**a**) Coherence coefficient diagram of Pair No. 1; (**b**) Coherence coefficient diagram of Pair No. 2; (**c**) Coherence coefficient diagram of Pair No. 3; (**d**) Coherence coefficient diagram of Pair No. 4; (**e**) Coherence coefficient diagram of Pair No. 5; (**f**) Coherence coefficient diagram of Pair No. 6; (**g**) Coherence coefficient diagram of Pair No. 7; (**h**) Coherence coefficient diagram of Pair No. 8; (**i**) Coherence coefficient diagram of Pair No. 9; (**j**) Coherence coefficient diagram of Pair No. 10; (**k**) Coherence coefficient diagram of Pair No. 11; (**l**) Coherence coefficient diagram of Pair No. 12.

A phase unwrapping algorithm was applied to the filter-enhanced differential interferometric phases, and the absolute phase values obtained through unwrapping were converted into surface deformation components along the radar line-of-sight direction. Using a spatial projection transformation model and geocoding technology, this slant-range deformation component was transformed into a vertical deformation field in the geodetic coordinate system. To reveal the temporal evolution pattern of the subsidence basin in the study area, subsidence values at each monitoring point for different time intervals were extracted and cumulatively summed to obtain the total subsidence from 18 January to 22 June 2024. The cumulative subsidence results of the mine area derived from InSAR are shown in Figure 9.

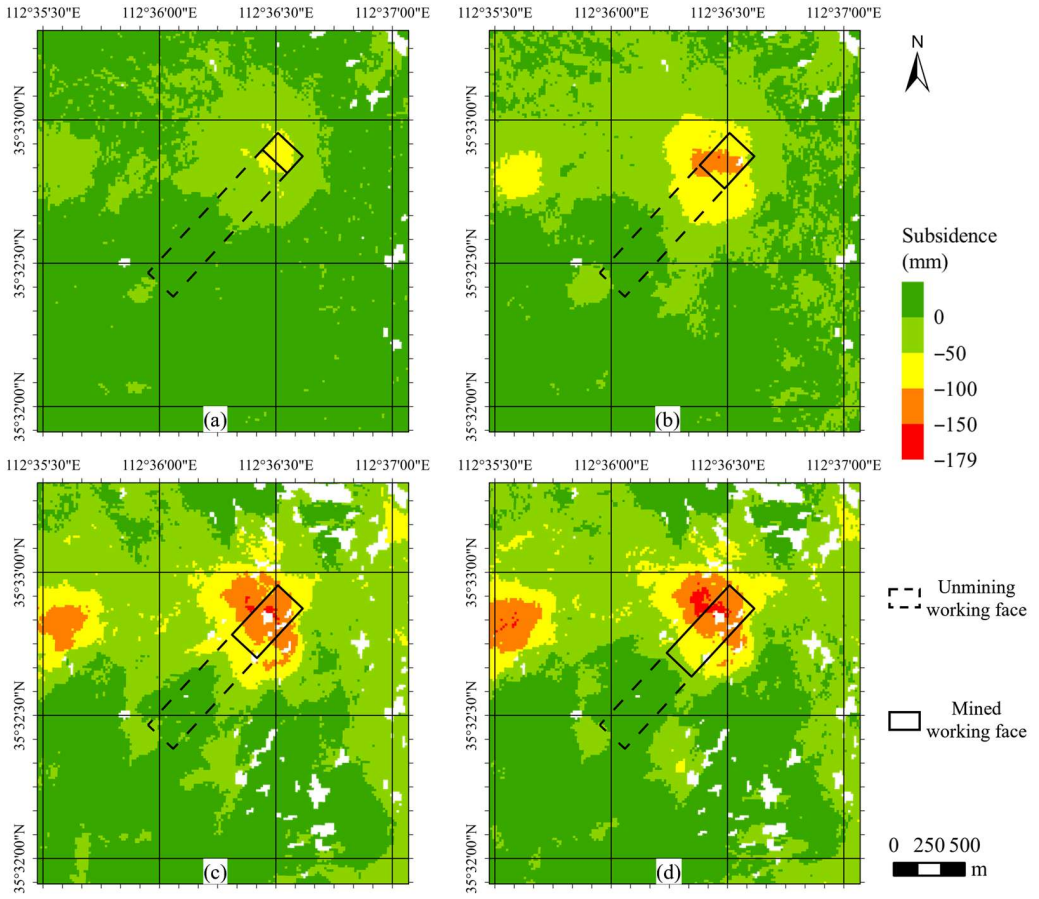


Figure 9. InSAR time series cumulative subsidence results: (**a**) Cumulative subsidence on 23 February 2024; (**b**) Cumulative subsidence on 30 March 2024; (**c**) Cumulative subsidence on 5 May 2024; (**d**) Cumulative subsidence on 22 June 2024.

As shown in Figure 9, with working face advancement, a funnel-shaped subsidence basin gradually formed in the mining area, indicating that surface subsidence occurred due to mining activities during the monitoring period. At the beginning of monitoring, the maximum cumulative subsidence was 31 mm. By June 22, the subsidence center was approximately 240 m from the center of the open pit, and the maximum cumulative subsidence increased to 179 mm. In contrast, results from the third-order leveling survey during the same period showed that the maximum cumulative subsidence reached 1209 mm (the subsidence center point Z17 was 260 m from the open-pit center). The complete subsidence basin reconstructed by interpolating missing values in Figure 9d using the inverse distance weighting method is shown in Figure 10a.

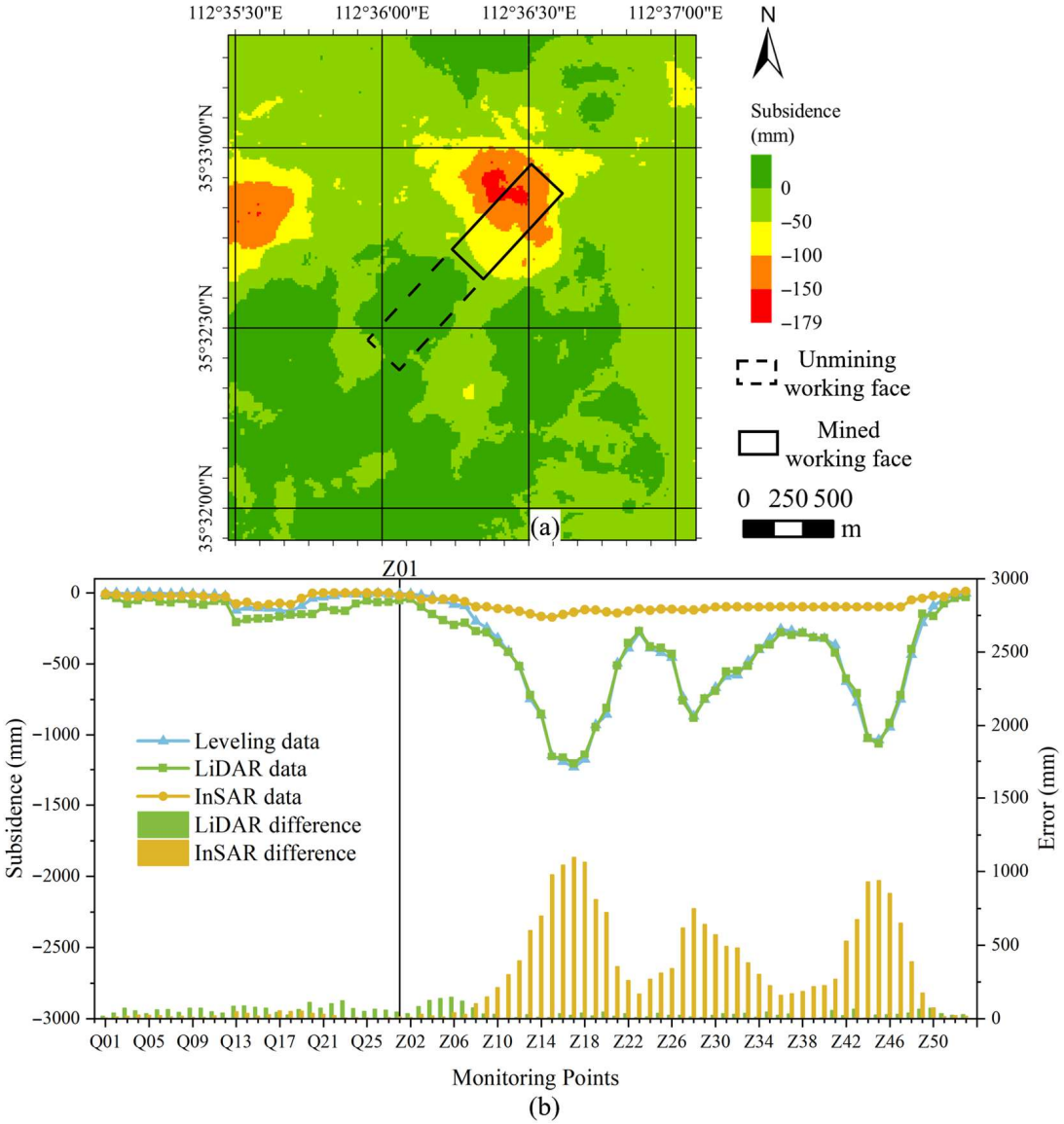


Figure 10. InSAR subsidence monitoring results and subsidence curve: (**a**) InSAR subsidence monitoring results; (**b**) InSAR and LiDAR subsidence curve.

3.2.2. LiDAR Monitoring Results and Analysis

For the complex environment of mountainous terrain with high undulation and high vegetation cover, the traditional filtering method has insufficient ground point extraction accuracy due to the dynamic interference of vegetation, which affects the subsidence monitoring accuracy. This study proposes a non-growing surface feature extraction algorithm based on the echo characteristics of LiDAR point clouds. The algorithm realizes the extraction of non-growing surface features such as roads and building roofs by analyzing the echo characteristics of multi-period LiDAR point cloud data.

In this study, CloudCompare software (version v2.14) was used to visualize the point cloud data of the study area, and a part of the study area was intercepted for subsequent processing. The CSF (Cloth Simulation Filtering) [38] method was adopted to extract ground points, with the following parameter settings: Steep slope, Cloth resolution = 2.000, Max iterations = 500, and Classification threshold = 0.500. The final extracted results of ground points are shown in Figure 11.

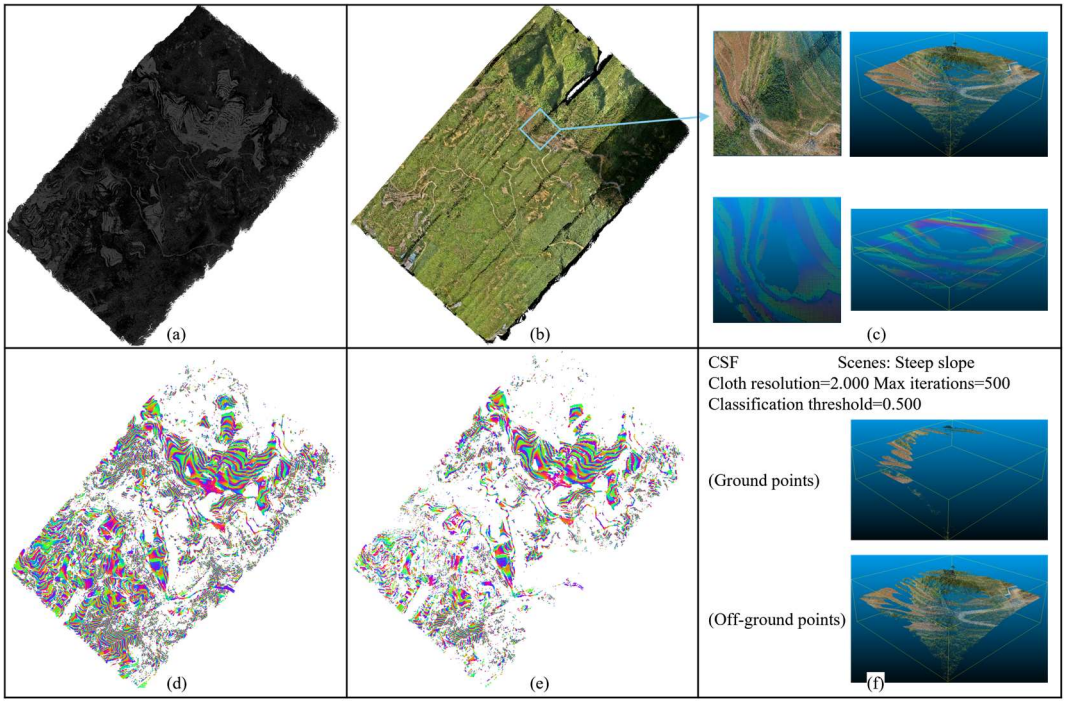


Figure 11. Non-growing surface feature extraction results: (**a**) Point cloud of 23 January 2024; (**b**) Point cloud of 22 June 2024; (**c**) Partial study area non-growing surface extraction results; (**d**) 23 January 2024 point cloud non-growing surface feature extraction results; (**e**) 22 June 2024 point cloud non-growing surface feature extraction results; (**f**) Partial study area CSF ground point extraction results.

As shown in Figure 11d,e, after processing with the CloudCompare Height Ramp module. The successful extraction of highways in the central part of the study area verifies the applicability of the non-ground surface feature extraction algorithm in flat regions, while the complete extraction of terraced landforms in the upper and lower parts of the study area confirms its favorable robustness to complex mountainous terrain.

As shown in Figure 11c,f, the conventional CSF algorithm fails to effectively extract ground points such as terraces and roads in this region, whereas the algorithm proposed in this study can achieve accurate extraction of such non-growing surface features.

Based on the two-phase non-growing surface features point cloud, 3D coordinate differences are calculated using the C2C algorithm. IDW (Inverse Distance Weighting) interpolation is then applied to fill data missing areas, constructing a complete subsidence basin model, and deriving subsidence curves along the strike and dip lines, as shown in Figures 10b and 12.

As shown in Figures 10b and 12, point cloud difference analysis of non-growing surface features based on the C2C algorithm reveals a significant subsidence basin in the working face, with its center approximately 270 m from the open-pit center and a maximum subsidence of 1209 mm, confirming that mining induces large-gradient surface deformation. Compared with third-order leveling, the subsidence center position basically matches, with a cumulative error of only 56 mm, verifying the accuracy of airborne LiDAR for monitoring large-gradient deformation in mining areas. Comparative analysis along the strike and dip lines shows that airborne LiDAR detects high-gradient deformation in the subsidence center significantly better than low-gradient deformation at the edge. The study demonstrates that airborne LiDAR can accurately invert the spatial distribution of large-gradient subsidence (deformation magnitude and center location) in mining areas, making it suitable for large-scale monitoring. However, small-gradient deformation zones

require integration with InSAR and other technologies to enable synergistic multiscale deformation monitoring across the entire area.

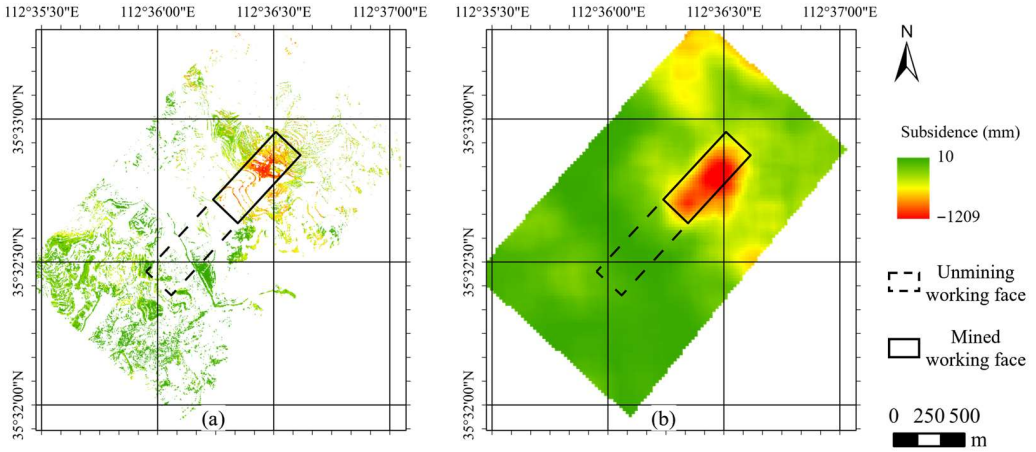


Figure 12. Airborne LiDAR subsidence monitoring results and subsidence curves: (**a**) C2C calculation results; (**b**) LiDAR subsidence monitoring results.

3.2.3. Fusion Monitoring Results

Statistics of coherence from 12 interferograms in the subsidence area (Table 3) show that coherence values in the mine subsidence area ranged from 0.377 to 0.629 between 18 January and 22 June 2024. Among them, SAR imagery coherence significantly decreased during spring–summer (April–June) due to rapid vegetation growth (γ_{avg} = 0.446), whereas in winter–spring (January–March), low vegetation coverage led to increased coherence (γ_{avg} = 0.557) and SAR imagery exhibited superior quality.

Table 3. Coherence statistics of 12 interferograms in the mining area.

Number	Primary Image	Auxiliary Image	Coherence Coefficient of the Subsidence Area
1	18 January 2024	30 January 2024	0.511
2	30 January 2024	11 February 2024	0.629
3	11 February 2024	23 February 2024	0.514
4	23 February 2024	6 March 2024	0.556
5	6 March 2024	18 March 2024	0.559
6	18 March 2024	30 March 2024	0.573
7	30 March 2024	11 April 2024	0.377
8	11 April 2024	23 April 2024	0.410
9	23 April 2024	5 May 2024	0.425
10	5 May 2024	17 May 2024	0.489
11	17 May 2024	10 June 2024	0.482
12	10 June 2024	22 June 2024	0.490

As shown in Table 3, the average coherence coefficient γ_{avg} of the 12 interferometric pairs in the study period is 0.501. Combining the spatial resolution of Sentinel-1A imagery (20 m × 20 m) with Equations (6) and (8), the maximum measurable deformation of InSAR, $d_{max\,|\,InSAR}$ is calculated as 97 mm. Using this threshold as a constraint, the complete subsidence basin model of the mine area is reconstructed by integrating InSAR subsidence data at the edge and probability integration method inversions for the center, as shown in Figure 13a.

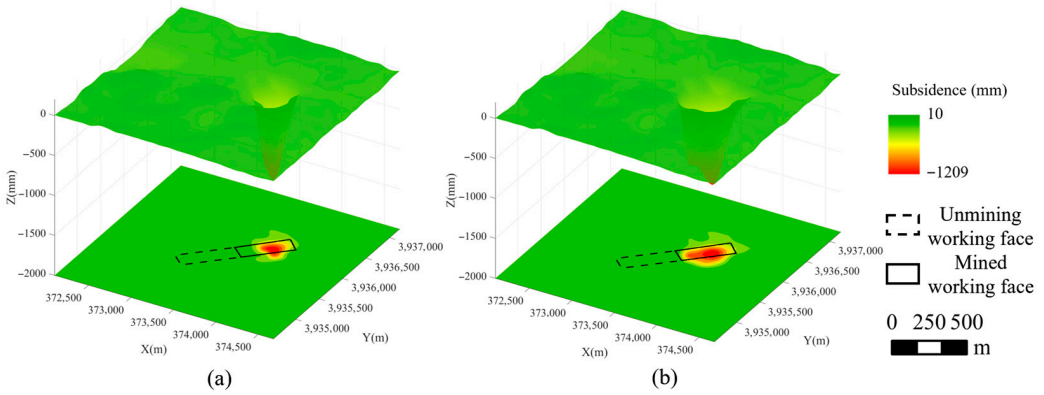


Figure 13. Weighted fusion of InSAR and LiDAR subsidence monitoring result: (**a**) Unweighted fusion subsidence results; (**b**) Weighted fusion subsidence results.

The average coherence coefficient γ_{avg} of 12 interferometric pairs in the InSAR monitoring data is 0.501. Interferometric pairs acquired during spring–summer (April–June) exhibit coherence degradation due to vegetation growth, affecting local monitoring accuracy. To improve data reliability, the first six interferometric pairs with coherence coefficients higher than the mean (γ_{avg} = 0.557) are selected. Combining Equations (5) and (7), the inverted maximum measurable deformation of InSAR, $d_{max\,|\,InSAR}$ is 62 mm.

To validate the weighted average method, 25 leveling points with subsidence between 62 mm and 414 mm are selected. For these points, absolute errors between InSAR/LiDAR monitoring values and leveling data are calculated, and the RMSE (Root Mean Square Errors) of InSAR and airborne LiDAR results are separately computed. The final RMSE values are 191 mm and 64 mm, respectively, as per Equation (8).

The fusion thresholds are set as follows: InSAR data are adopted when the subsidence is less than 62 mm, and LiDAR data are used when the subsidence exceeds 414 mm (this value is determined by the average subsidence of airborne LiDAR near the open-off cut). Combined with Equation (8), the weighting coefficients of P_{InSAR} and P_{LiDAR} are calculated as 0.251 and 0.749, respectively. For subsidence values between the two thresholds, the inversion results of InSAR and those of the probability integration method are weighted and fused using Equation (9) based on the proposed weighting model, as follows:

$$d = \begin{cases} d_{InSAR} & d < 62\text{mm} \\ 0.251 d_{InSAR} + 0.749 d_{LiDAR} & 61.7\text{ mm} \leqslant d \leqslant 414\text{mm}, \\ d_{LiDAR} & d > 414\text{mm} \end{cases} \quad (10)$$

Based on the weighted fusion calculation, the complete mine subsidence basin is presented in Figure 11.

Comparison between Figure 13a,b shows that fusing InSAR and LiDAR data reconstructs the complete spatial distribution of subsidence in the mining area. However, LiDAR monitoring reveals that the actual subsidence basin range along the working face advancing direction is wider than the InSAR results, leading to discontinuities in the subsidence boundary. To address this, weighted fusion of InSAR and LiDAR data is applied to the subsidence boundary area.

As shown in Figure 13, the fusion method resolves subsidence boundary discontinuities through weighted fusion of InSAR and LiDAR data. Compared with single techniques, the fusion method captures subsidence trends over a larger area and restores details of the subsidence center and boundary by combining InSAR's wide-area coverage with LiDAR's high precision, yielding more comprehensive and accurate monitoring results.

4. Discussion

4.1. Accuracy Assessment of Monitoring Results

To verify the weighted fusion method's accuracy, 80 points (Z1-Z53 and Q1-Q27) near the working face were selected to extract deformation values from InSAR, LiDAR, and the weighted fusion method. Third-order leveling measurements of corresponding points were used for quantitative accuracy assessment. Deformation thresholds were classified as small gradient (<62 mm), medium gradient (62 mm to 414 mm), and large gradient (>414 mm). Monitoring errors of InSAR, LiDAR, and the weighted fusion method in each gradient area are shown in Table 4 and Figure 14.

Table 4. Monitoring error statistics of three methods.

Gradient	Monitoring Method	RMSE/mm	MAE/mm	Max AE/mm
Large gradient	InSAR	707	665	1096
	LiDAR	29	25	65
	Weighted fusion	29	25	65
Medium gradient	InSAR	172	144	306
	LiDAR	60	46	145
	Weighted fusion	45	34	118
Small gradient	InSAR	17	15	367
	LiDAR	70	62	138
	Weighted fusion	17	15	37
Full gradient	InSAR	415	268	1096
	LiDAR	56	45	145
	Weighted fusion	39	29	118

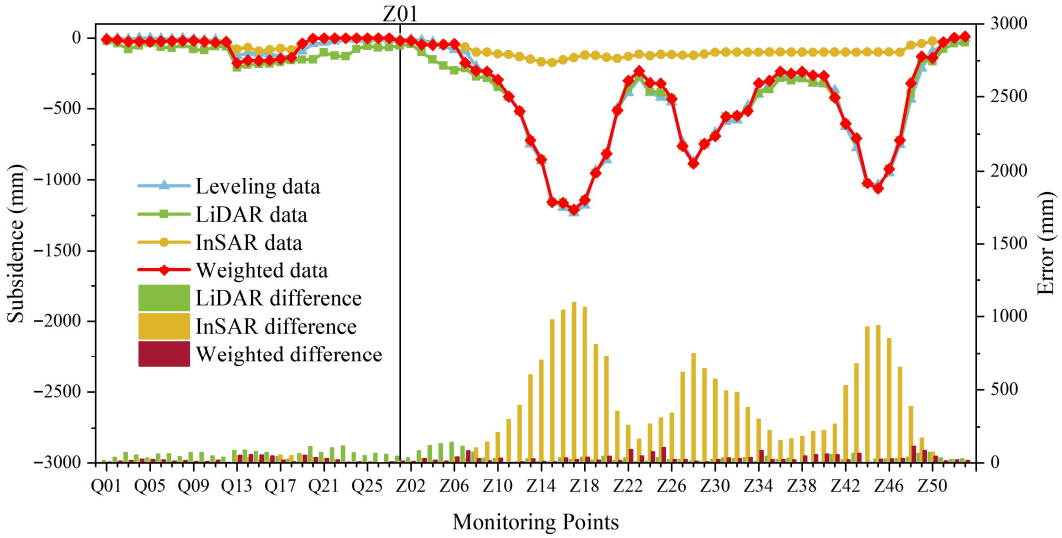


Figure 14. Comparison of monitoring errors among the three methods.

Three indicators were adopted for accuracy evaluation: RMSE (root mean square error) reflects the dispersion between monitored and true values, indicating method stability; MAE (mean absolute error) represents the overall deviation level; Max AE (maximum absolute error) characterizes the upper limit of extreme deviation.

From the analysis of Figure 14 and Table 4, it can be concluded that:

(1) InSAR exhibited outstanding performance in small-gradient deformation zones, with an RMSE of 17 mm, MAE of 15 mm, and Max AE of 37 mm, which were

73–76% lower than those of LiDAR in the same zone. In medium-gradient zones, the accuracy degraded obviously, with an RMSE of 172 mm, MAE of 144 mm, and Max AE of 306 mm. In large-gradient subsidence centers, InSAR suffered from severe phase decorrelation and failed completely, yielding an RMSE of 707 mm, MAE of 665 mm, and Max AE of 1096 mm. For the full-gradient range, InSAR achieved an RMSE of 415 mm and MAE of 268 mm, showing poor adaptability to large-gradient deformations.

(2) LiDAR showed superior accuracy in large-gradient zones, with an RMSE of 29 mm, MAE of 25 mm, and Max AE of 65 mm, which were 94–96% lower than those of InSAR. In medium-gradient zones, LiDAR maintained stable performance with an RMSE of 60 mm, MAE of 46 mm, and Max AE of 145 mm, outperforming InSAR but inferior to the weighted fusion method. In small-gradient zones, LiDAR had insufficient precision, with an RMSE of 70 mm, MAE of 62 mm, and Max AE of 138 mm, which were 73–76% higher than those of InSAR. For the full-gradient range, LiDAR obtained an RMSE of 56 mm and MAE of 45 mm, better than InSAR but limited in small-gradient monitoring.

(3) The weighted fusion method adopted a gradient strategy: InSAR for small gradients, LiDAR for large gradients, and weighted fusion for medium gradients. In large-gradient zones, it maintained the high accuracy of LiDAR. In medium-gradient zones, it achieved significant accuracy improvement, superior to both single techniques. In small-gradient zones, it retained the high precision of InSAR. For the full-gradient range, the weighted fusion method reduced the RMSE to 39 mm, which were 91% lower than those of InSAR and 30% lower than those of LiDAR.

4.2. Echo Threshold Determination

This study focuses on extracting non-growing feature point clouds and determining the grid echo ratio threshold. A plain campus area (Test A) with roads, building roofs, and bare soil, and a mountainous extraction area (Test B) with snow-covered roads and bare soil, were selected as test sites to compare the effects of terrain differences. As shown in Figure 15, three sets of echo thresholds (0% (a2, b2), 10% (a3, b3), and 20% (a4, b4)) were used for comparative point cloud extraction analysis. Table 5 lists the number of extracted non-growing feature points for each threshold.

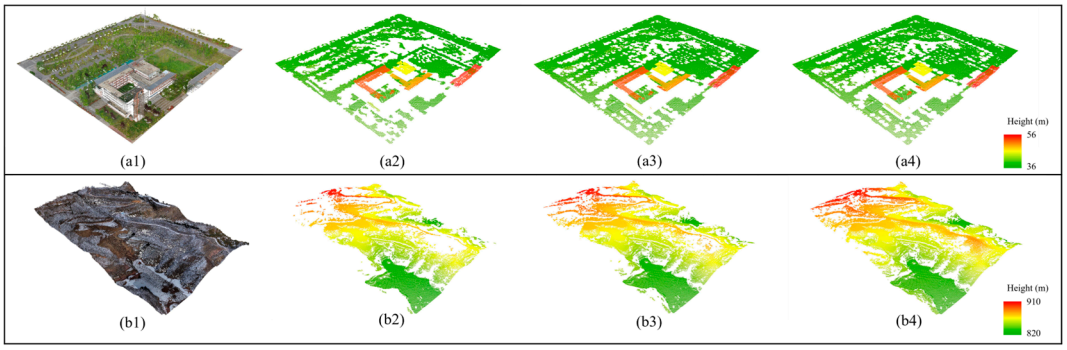


Figure 15. Colored point cloud and echo ratio threshold analysis: (**a1**) Original point cloud of Test A; (**a2**) Extracted non-growing feature points in Test A with 0% echo threshold; (**a3**) Extracted non-growing feature points in Test A with 10% echo threshold; (**a4**) Extracted non-growing feature points in Test A with 20% echo threshold; (**b1**) Original point cloud of Test B; (**b2**) Extracted non-growing feature points in Test B with 0% echo threshold; (**b3**) Extracted non-growing feature points in Test B with 10% echo threshold; (**b4**) Extracted non-growing feature points in Test B with 20% echo threshold.

Table 5. Extracted points of non-growing surface features by echo threshold.

Echo Threshold/%	Number of Extraction Points in Test A	Number of Extraction Points in Test B
0	35,474	125,916
10	42,936	151,110
20	43,006	159,594

Comparison of Figure 15 and Table 5 reveals that the number of extracted non-growing feature points decreases significantly as the echo ratio threshold increases from 0% to 10%. When the threshold increases to 20%, the point count decrease tends to slow, indicating that the 10% threshold approaches the convergence point for optimal extraction.

To verify the reliability of the proposed method, a public dataset named District of Columbia—Classified Point Cloud LiDAR https://registry.opendata.aws/dc-lidar-2015 (accessed on 20 April 2026) was selected for the control experiment. The classical CSF algorithm was adopted to extract ground points with the following parameter settings: terrain type = Relief, cloth resolution = 2.000, maximum iterations = 500, and classification threshold = 0.500. The final ground point extraction results are presented in Figure 16.

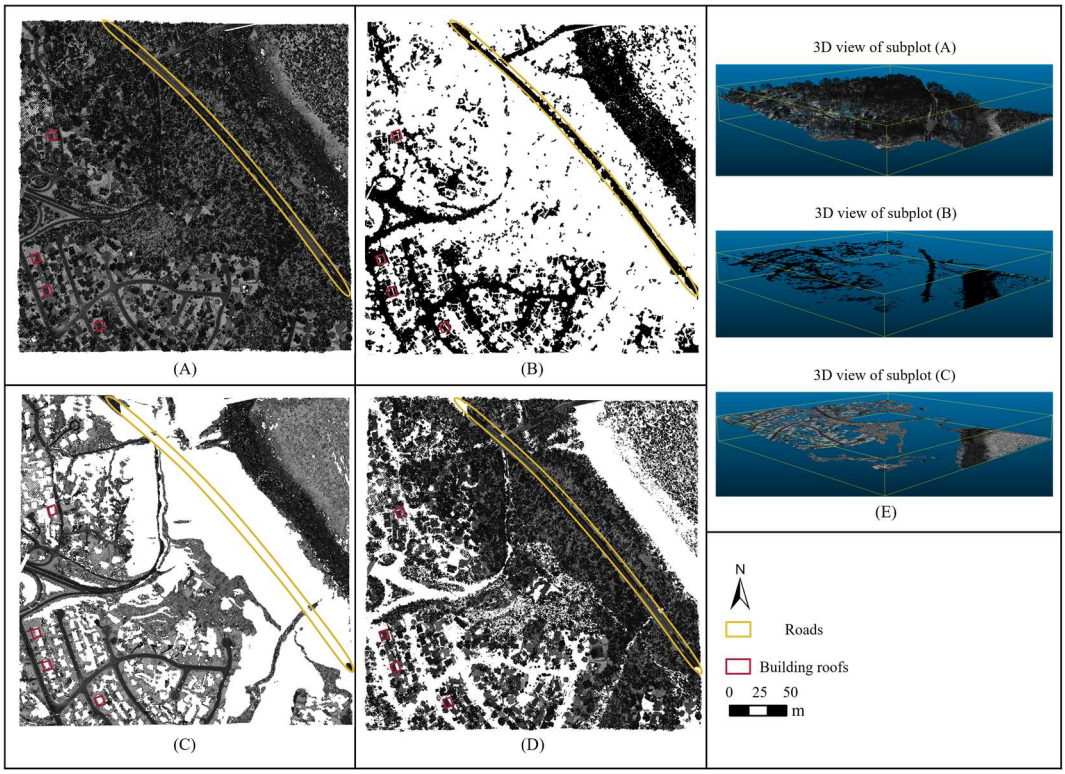


Figure 16. Experimental results of public dataset: (**A**) Original LiDAR point cloud data; (**B**) non-growing surface feature extraction results; (**C**) CSF ground point extraction results; (**D**) CSF non-ground point extraction results; (**E**) 3D view.

As shown in Figure 16, the selected public dataset contains various features such as buildings, roads, and vegetation, with relatively complex terrain conditions. The non-growing surface feature extraction results obtained using the method proposed in this paper are shown in Figure 10b, where roads and building roofs can be completely extracted. In contrast, the extraction results of the traditional CSF algorithm, as illustrated in Figure 16C, exhibit severe loss of road information and misclassification and removal of buildings. This indicates that conventional ground point filtering algorithms are prone to erroneous feature elimination and loss of key information in complex urban scenarios, whereas the

proposed method can retain non-growing surface features such as roads and buildings more accurately, demonstrating stronger applicability and reliability in the complex mountainous terrain of western China.

5. Conclusions

This study proposes an InSAR and LiDAR fusion method that leverages LiDAR echo characteristics to extract non-growing surface features and uses InSAR deformation gradient theory to define fusion boundaries. The weighted fusion strategy realizes reliable integration in medium-gradient zones.

Engineering experiments demonstrate that the weighted fusion method achieves centimeter-level accuracy across the entire subsidence basin. It retains high precision in both large-gradient centers and small-gradient edges, reducing the full-gradient RMSE to 39 mm—91% lower than InSAR and 30% lower than LiDAR.

The proposed method effectively overcomes the limitations of single remote sensing techniques and provides a scalable technical framework for high-precision subsidence monitoring in western Chinese mining areas. Future work will focus on optimizing fusion parameters to adapt to diverse mining terrains, conducting threshold sensitivity analysis, and evaluating cross-site transferability to further enhance the method's universality and robustness.

Author Contributions: D.X.: Data Curation, Methodology, Validation, Writing—Original Draft, Visualization, Project administration. T.W.: Funding acquisition, Writing—original draft, Writing—Review & Editing. L.W.: Conceptualization, Funding acquisition, Methodology, Resources, Supervision, Writing—review and editing. J.L.: Data Curation, Validation. S.C.: Funding acquisition, Writing—review and editing. X.L.: Data Curation, Investigation. All authors have read and agreed to the published version of the manuscript.

Funding: This work was financially supported by the National Natural Science Foundation of China (grant number 52474194, 52504186) and the Scientific Research Foundation for High-level Talents of Anhui University of Science and Technology (grant number 2024yjrc63).

Data Availability Statement: The data that support the findings of this study are available from the corresponding author upon reasonable request.

Conflicts of Interest: Author Dayong Xu was employed by Cathay Safety Technology Co., Ltd., Beijing 102299, China. The remaining authors declare that the research was conducted in the absence of any commercial or financial relationships that could be construed as a potential conflict of interest.

Abbreviations

The following abbreviations are used in this manuscript:

InSAR	Interferometric Synthetic Aperture Radar
LiDAR	Light Detection and Ranging
C2C	Cloud-to-Cloud
DEM	Digital Elevation Model
IDW	Inverse Distance Weighting
SLC	Single Look Complex
POD	Precision Orbit Determination
GACOS	Generic Atmospheric Correction Online Service
UAV	Unmanned Aerial Vehicle
RTK	Real-Time Kinematic
VV	Vertical–Vertical Polarization
ESA	European Space Agency
NASA	National Aeronautics and Space Administration
RMSE	Root Mean Square Error

References

1. Xiao, Y.; Yang, H.; Xiang, X.; Li, Z.; Zhang, L. Lifting or lessening? Examining the effect of low-carbon city trial on synergistic reduction of pollution and carbon emissions. *Energy* **2025**, *314*, 134195. [CrossRef]
2. Wu, H.A.; Zhang, Y.; Sun, X.; Liu, Y.; Lu, Z.; Kang, Y.; Wei, J.; Yang, K.; Li, L.; Liu, N.; et al. A traceability investigation of the 2023 Xinjing open-pit coal mine landslide: Remote sensing analysis using spaceborne SAR and optical imagery. *Landslides* **2026**, *23*, 399. [CrossRef]
3. Cao, X.; Liu, C.; Wu, M.; Li, Z.; Wang, Y.; Wen, Z. Heterogeneity and connection in the spatial–temporal evolution trend of China's energy consumption at provincial level. *Appl. Energy* **2023**, *336*, 120842. [CrossRef]
4. Zhan, H.; Liu, S.; Wu, Q.; Liu, W.; Shi, L.; Liu, D. Effects of deep coal mining on groundwater hydrodynamic and hydrochemical processes in a multi-aquifer system: Insights from a long-term study of mining areas in ecologically fragile western China. *J. Contam. Hydrol.* **2024**, *265*, 104386. [CrossRef]
5. Du, Q.; Guo, G.; Zhang, L.; Li, H.; Zheng, H.; Meng, F.; Wei, T. Analyzing the subsidence pattern of deep mining in ecologically fragile areas of western China. *KSCE J. Civ. Eng.* **2025**, *29*, 100136. [CrossRef]
6. Sun, Q.; Bai, R.; Fan, L.; Jiang, Y.; Zhou, N.; Zhang, J. Sustainable high-intensity backfill coal mining method: Feasibility assessment for ecologically fragile areas of Western China. *Energy Sources Part A Recovery Util. Environ. Eff.* **2022**, *44*, 7764. [CrossRef]
7. Guo, H.; Ji, M.; Zhao, W. Analysis of the distribution characteristics and laws of in situ stress in China's coal mines. *Arab. J. Geosci.* **2020**, *13*, 478. [CrossRef]
8. Fernández-Manso, A.; Quintano, C.; Roberts, D. Evaluation of potential of multiple endmember spectral mixture analysis (MESMA) for surface coal mining affected area mapping in different world forest ecosystems. *Remote Sens. Environ.* **2012**, *127*, 181. [CrossRef]
9. Xiao, W.; Ren, H.; Sui, T.; Zhang, H.; Zhao, Y.; Hu, Z. A drone-and field-based investigation of the land degradation and soil erosion at an opencast coal mine dump after 5 years' evolution of natural processes. *Int. J. Coal Sci. Technol.* **2022**, *9*, 42. [CrossRef]
10. Geng, J.; Li, Q.; Li, X.; Zhou, T.; Liu, Z.; Xie, Y. Research on the Evolution Characteristics of Rock Mass Response from Open-Pit to Underground Mining. *Adv. Mater. Sci. Eng.* **2021**, *2021*, 3200906. [CrossRef]
11. Li, Y.; Zuo, X.; Xiong, P.; You, H.; Zhang, H.; Yang, F.; Zhao, Y.; Yang, Y.; Liu, Y. Deformation monitoring and analysis of Kunyang phosphate mine fusion with InSAR and GPS measurements. *Adv. Space Res.* **2022**, *69*, 2637. [CrossRef]
12. Dai, M.; Li, H.; Long, B.; Wang, X. Quantitative identification of landslide hazard in mountainous open-pit mining areas combined with ascending and descending orbit InSAR technology. *Landslides* **2024**, *21*, 2975. [CrossRef]
13. Ma, J.; Yang, J.; Zhu, Z.; Cao, H.; Li, S.; Du, X. Decision-making fusion of InSAR technology and offset tracking to study the deformation of large gradients in mining areas-Xuemiaotan mine as an example. *Front. Earth Sci.* **2022**, *10*, 962362. [CrossRef]
14. Antonielli, B.; Sciortino, A.; Scancella, S.; Bozzano, F.; Mazzanti, P. Tracking Deformation Processes at the Legnica Glogow Copper District (Poland) by Satellite InSAR—I: Room and Pillar Mine District. *Land* **2021**, *10*, 653. [CrossRef]
15. Wang, Y.; Cui, X.; Che, Y.; Zhao, Y.; Li, P.; Kang, X.; Jiang, Y. Near Real-Time Monitoring of Large Gradient Nonlinear Subsidence in Mining Areas: A Hybrid SBAS-InSAR Method Integrating Robust Sequential Adjustment and Deep Learning. *Remote Sens.* **2024**, *16*, 1664. [CrossRef]
16. Quan, L.; Long, Z.; Ma, Z.A.; Chen, K.; Chen, X.; Xu, Y.; Liu, J. Method of Monitoring Three-dimensional Mining Surface Deformation Based on InSAR. *Meteorol. Environ. Res.* **2024**, *15*, 72. [CrossRef]
17. Long, S.; Liu, M.; Xiong, C.; Li, T.; Wu, W.; Ding, H.; Zhang, L.; Zhu, C.; Lu, S. Research on prediction of surface deformation in mining areas based on TPE-optimized integrated models and multi-temporal InSAR. *Remote Sens.* **2023**, *15*, 5546. [CrossRef]
18. Zhang, L.; Gao, P.; Gan, Z.; Wu, W.; Sun, Y.; Zhu, C.; Peng, H. Subsidence monitoring of mining areas in Hunan province based on Sentinel-1A and DS-InSAR. *Sensors* **2023**, *23*, 8146. [CrossRef]
19. Zhang, L.; Cai, X.; Wang, Y.; Wei, W.; Liu, B.; Jia, S.; Pang, T.; Bai, F.; Wei, Z. Long-term ground multi-level deformation fusion and analysis based on a combination of deformation prior fusion model and OTD-InSAR for longwall mining activity. *Measurement* **2020**, *161*, 107911. [CrossRef]
20. Kissling, W.D.; Shi, Y.; Wang, J.; Walicka, A.; George, C.; Moeslund, J.E.; Gerard, F. Towards consistently measuring and monitoring habitat condition with airborne laser scanning and unmanned aerial vehicles. *Ecol. Indic.* **2024**, *169*, 112970. [CrossRef]
21. Zhong, W.; Chu, T.; Tissot, P.; Wu, Z.; Chen, J.; Zhang, H. Integrated coastal subsidence analysis using InSAR, LiDAR, and land cover data. *Remote Sens. Environ.* **2022**, *282*, 113297. [CrossRef]
22. Liu, Y.; Obukhov, A.; Wegner, J.D.; Schindler, K. Point2Building: Reconstructing buildings from airborne LiDAR point clouds. *ISPRS J. Photogramm. Remote Sens.* **2024**, *215*, 351. [CrossRef]
23. Ordóñez, C.; Calvopiña, J.; Toapanta, S.; Carranco, A.; González, J. Integrating lidar technology in artisanal and small-scale mining: A comparative study of iPad Pro LiDAR sensor and traditional surveying methods in Ecuador's artisanal gold mine. *J. Geod. Sci.* **2024**, *14*, 20220181. [CrossRef]

24. Yang, Q.; Tang, F.; Wang, F.; Tang, J.; Fan, Z.; Ma, T.; Su, Y.; Xue, J. A new technical pathway for extracting high accuracy surface deformation information in coal mining areas using UAV LiDAR data: An example from the Yushen mining area in western China. *Measurement* **2023**, *218*, 113220. [CrossRef]
25. Zheng, J.; Yao, W.; Lin, X.; Ma, B.; Bai, L. An accurate digital subsidence model for deformation detection of coal mining areas using a UAV-based LiDAR. *Remote Sens.* **2022**, *14*, 421. [CrossRef]
26. Pawluszek-Filipiak, K.; Borkowski, A. Integration of DInSAR and SBAS Techniques to determine mining-related deformations using sentinel-1 data: The case study of Rydułtowy mine in Poland. *Remote Sens.* **2020**, *12*, 242. [CrossRef]
27. Zhu, M.; Yu, X.; Tan, H.; Yuan, J. Integrated high-precision monitoring method for surface subsidence in mining areas using D-InSAR, SBAS, and UAV technologies. *Sci. Rep.* **2024**, *14*, 12445. [CrossRef] [PubMed]
28. Bailey, G.; Li, Y.; McKinney, N.; Yoder, D.; Wright, W.; Herrero, H. Comparison of ground point filtering algorithms for high-density point clouds collected by terrestrial LiDAR. *Remote Sens.* **2022**, *14*, 4776. [CrossRef]
29. Chen, C.; Guo, J.; Wu, H.; Li, Y.; Shi, B. Performance comparison of filtering algorithms for high-density airborne LiDAR point clouds over complex LandScapes. *Remote Sens.* **2021**, *13*, 2663. [CrossRef]
30. Yan, Y.; Wang, H.; Song, B.; Chen, Z.; Fan, R.; Chen, D.; Dong, Z. Airborne Streak Tube Imaging LiDAR Processing System: A Single Echo Fast Target Extraction Implementation. *Remote Sens.* **2023**, *15*, 1128. [CrossRef]
31. Shi, T.; Zhong, D.; Bi, L. A new challenge: Detection of small-scale falling rocks on transportation roads in open-pit mines. *Sensors* **2021**, *21*, 3548. [CrossRef] [PubMed]
32. Sui, H.; Asaba, K.; Sakai, K.; Miyanaga, S.; Cui, Y. Assessment of C2C-based point cloud comparison errors based on distribution characteristics of tunnel point clouds. *Int. J. Remote Sens.* **2025**, *46*, 2646–2664. [CrossRef]
33. Yin, H.; Guo, G.; Li, H.; Wang, T. A prediction model of mining subsidence based on an unskewed continuous probability distribution over an infinite interval. *Environ. Earth Sci.* **2024**, *83*, 467. [CrossRef]
34. Gilanipoor, A.; Motevalli, S.; Ghobadi, G.J.; Derafshi, K. Investigating the effects of climatic elements on landslides using multi-temporal DInSAR technology and statistical analysis. *Theor. Appl. Climatol.* **2025**, *156*, 649. [CrossRef]
35. Yasir, M.; Casu, F.; De Luca, C.; Onorato, G.; Lanari, R.; Manunta, M. An innovative minimum cost flow phase unwrapping algorithm based on compressive sensing for multi-temporal small baseline DInSAR interferograms sequences. *ISPRS J. Photogramm. Remote Sens.* **2026**, *236*, 120. [CrossRef]
36. Massonnet, D.; Feigl, K.L. Radar interferometry and its application to changes in the Earth's surface. *Rev. Geophys.* **1998**, *36*, 441. [CrossRef]
37. Baran, I.; Stewart, M.; Claessens, S. A new functional model for determining minimum and maximum detectable deformation gradient resolved by satellite radar interferometry. *IEEE Trans. Geosci. Remote Sens.* **2005**, *43*, 675. [CrossRef]
38. Zhang, W.; Qi, J.; Wan, P.; Wang, H.; Xie, D.; Wang, X.; Yan, G. An Easy-to-Use Airborne LiDAR Data Filtering Method Based on Cloth Simulation. *Remote Sens.* **2016**, *8*, 501. [CrossRef]

Disclaimer/Publisher's Note: The statements, opinions and data contained in all publications are solely those of the individual author(s) and contributor(s) and not of MDPI and/or the editor(s). MDPI and/or the editor(s) disclaim responsibility for any injury to people or property resulting from any ideas, methods, instructions or products referred to in the content.